Computation of the linear elastic properties of random porous materials with a wide variety of microstructure

by

A. P. Roberts
Centre for Microscopy and Microanalysis
University of Queensland
St. Lucia, Queensland 4072 AUSTRALIA

and

E. J. Garboczi
Building and Fire Research Laboratory
National Institute of Standards and Technology
Gaithersburg, MD 20899 USA

Reprinted from the Proceedings of the Royal Society of London, Series A - Mathematical, Physical and Engineering Sciences, Vol. 458, No. 2021, 1033-1054, 2002.

NIST
National Institute of Standards and Technology
Technology Administration, U.S. Department of Commerce

10.1098/rspa.2001.0900

THE ROYAL SOCIETY

Computation of the linear elastic properties of random porous materials with a wide variety of microstructure

By A. P. Roberts[1,2] and E. J. Garboczi[1]

[1]*Building Materials Division, National Institute of Standards and Technology, Gaithersburg, MD 20899, USA*
(anthony.roberts@mailbox.uq.edu.au; edward.garboczi@nist.gov)
[2]*Centre for Microscopy and Microanalysis, University of Queensland, St Lucia, Queensland 4072, Australia*

Received 28 March 2001; accepted 30 July 2001; published online 3 April 2002

A finite-element method is used to study the elastic properties of random three-dimensional porous materials with highly interconnected pores. We show that Young's modulus, E, is practically independent of Poisson's ratio of the solid phase, ν_s, over the entire solid fraction range, and Poisson's ratio, ν, becomes independent of ν_s as the percolation threshold is approached. We represent this behaviour of ν in a flow diagram. This interesting but approximate behaviour is very similar to the exactly known behaviour in two-dimensional porous materials. In addition, the behaviour of ν versus ν_s appears to imply that information in the dilute porosity limit can affect behaviour in the percolation threshold limit. We summarize the finite-element results in terms of simple structure–property relations, instead of tables of data, to make it easier to apply the computational results.

Without using accurate numerical computations, one is limited to various effective medium theories and rigorous approximations like bounds and expansions. The accuracy of these equations is unknown for general porous media. To verify a particular theory it is important to check that it predicts both isotropic elastic moduli, i.e. prediction of Young's modulus alone is necessary but not sufficient. The subtleties of Poisson's ratio behaviour actually provide a very effective method for showing differences between the theories and demonstrating their ranges of validity. We find that for moderate- to high-porosity materials, none of the analytical theories is accurate and, at present, numerical techniques must be relied upon.

Keywords: structure–property relationships; theoretical mechanics; porous media; elasticity; percolation

1. Introduction

A central goal in the study of materials is to understand and quantify the relationship between the internal structure of materials and their properties. Structure–property relationships are used for designing and improving materials or, conversely, for interpreting experimental relationships in terms of microstructural features. Ideally, the aim is to construct a theory that employs general microstructural information to

make accurate property predictions. A less ambitious, but more likely, goal is the provision of structure–property relations for different classes of microstructure.

Significant progress towards this goal has been made for the linear elastic properties of random porous media. Relevant reviews of the topic have been made by Hashin (1983) and Torquato (1991). If the pores are isolated, can be approximated by spheroids and occupy low-to-moderate volume fractions, a variety of effective medium and rigorous approximations provide good predictions. These types of materials can be termed *dispersions*. However, many porous materials have a more *interconnected* or *interpenetrating* structure. Even at low porosities, the pores can form large clusters, while at higher porosities the pore phase can be macroscopically interconnected, giving a bi-continuous structure. Currently, no practical theory exists that is guaranteed to accurately predict the properties of random interpenetrating porous media. For example, the predictions of effective medium theories were 25% higher than data for a porous model with just 20% porosity (Roberts & Garboczi 1999). In this paper we address this deficiency by computing empirical structure property relations for porous media with a wide variety of microstructures.

A number of theoretical formulae have been proposed that are relevant to interpenetrating porous media. For example, effective medium theories (Hashin 1983) were developed to extend exact results for dilute inclusions to higher volume fractions. Certain microstructures were shown *a posteriori* (Milton 1984) to have properties that correspond to the theories, but the physical structures are very unusual. A different class of theories is rigorously based on realistic microstructural information. These are the classic variational bounds (Milton & Phan-Thien 1982), which only provide an upper bound for porous media, and the recent expansion of Torquato (1998). The microstructural information needed to evaluate the results is quite difficult to obtain, so in practice the bounds and expansion are evaluated at 'third order'. Even with limited information, the upper bounds and expansions are thought to give good predictions for dispersions (Torquato 1991, 1998, § 3.5). The accuracy of either class of theories is not possible to determine *a priori* for realistic interpenetrating porous media, so it is difficult to use the results to either improve a material or interpret experimental data. This uncertainty has limited the application of the results. Nevertheless, effective medium theories are commonly used, and the rigorous theories are attractive because of their relatively simplicity (compared with computation). Therefore, it would be extremely useful to establish the conditions and realistic microstructure types for which the theories do make accurate predictions. To address this question, on a model-by-model basis, we compare various well-known theories to our numerical data. However, to verify a particular theory, it is important to check that it predicts both isotropic elastic moduli, i.e. prediction of Young's modulus alone is necessary but not sufficient (even though this is usually the only parameter measured!). The subtleties of the Poisson ratio behaviour actually provide a very effective method for showing differences between the theories and demonstrating their ranges of validity. These subtleties will be described later in the paper.

The macroscopic elastic properties of two- and three-dimensional isotropic porous materials can be characterized by two independent constants, Young's modulus (E) and Poisson's ratio (ν). In general, we expect the elastic constants to depend on properties of the solid matrix (which we denote with subscript s), or $E = E_s f(p, \nu_s)$ and $\nu = g(p, \nu_s)$. Here, p is the relative density or solid volume fraction, and the form

of the dimensionless functions f and g depends on microstructure. In two dimensions it has been observed that f and g have two remarkable properties for arbitrary porous materials (Day *et al.* 1992). First, Young's modulus is independent of ν_s, or $f(p, \nu_s) = f(p)$. Second, if the solid fraction decreases to the percolation threshold p_c, the effective Poisson ratio converges to a fixed point independent of the solid Poisson ratio, or $g(p, \nu_s) \to \nu_1$ as $p \to p_c$. Both results were subsequently proved analytically by Cherkaev *et al.* (1992) (CLM) and Thorpe & Jasiuk (1992). Christensen (1993) has pointed out that although E cannot be independent of ν_s in three dimensions, it is nearly so for materials with dilute spheroidal voids over a restricted range of Poisson's ratio $0 \leqslant \nu_s \leqslant 0.5$. Variational bounds and approximate self-consistent theories showed a similar weak dependence of E on ν_s (for $0 \leqslant \nu_s \leqslant 0.5$) over the full range of solid fraction $0 \leqslant p \leqslant 1$. Since the CLM theorem, which is only true in two dimensions, was used to prove the existence of the fixed point for ν in two dimensions (Thorpe & Jasiuk 1992), this behaviour is not thought to hold rigorously in three dimensions. However, it is interesting to examine how well these inherently two-dimensional results, both for E and for ν, do approximately hold in three dimensions.

2. Theoretical structure–property relationships

(*a*) *Dilute limits and effective medium theory*

One of the few exact structure–property results in three dimensions is for a dilute concentration of spheroidal inclusions with bulk and shear moduli K_i and G_i dispersed in a solid matrix with moduli K_s and G_s. In this case, where unsubscripted variables stand for effective quantities (Hashin 1983),

$$K = K_s + c_i P^{si}(K_i - K_s), \tag{2.1}$$

$$G = G_s + c_i Q^{si}(G_i - G_s). \tag{2.2}$$

Here, $c_i = 1 - p$ denotes the concentration (volume fraction) of inclusions and, for the case of spherical inclusions,

$$P^{si} = \frac{3K_s + 4G_s}{3K_i + 4G_s}, \qquad Q^{si} = \frac{G_s + F_s}{G_i + F_s}, \qquad F_s = \frac{G_s}{6}\frac{9K_s + 8G_s}{K_s + 2G_s}. \tag{2.3}$$

The form of P^{si} and Q^{si} for spheroidal inclusions (Wu 1966) is given by Berryman (1980). Young's modulus and Poisson's ratio are obtained via the relations $E = 9KG/(3K + G)$ and $\nu = (3K - 2G)/(6K + 2G)$. When the inclusions are pores, ν exhibits the interesting property that $\nu = 0.2$ when $\nu_s = 0.2$ for any value of E. This has been shown before (Garboczi & Day 1995). In two dimensions, the equivalent value is $\frac{1}{3}$.

To adapt the dilute formulae to the case of a finite concentration of inclusions, a number of proposals have been made. The approximate equations that result are usually called effective medium theories. The most common approximation is the so-called self-consistent method (SCM) of Hill (1965) and Budiansky (1965). In this model, the equations of elasticity are solved for a spherical inclusion embedded in a medium of unknown effective moduli. The effective moduli K and G are then derived. In the dilute case, the embedding medium is just the matrix. The Hill–Budiansky

result can be stated as (Berryman 1980)

$$c_{\rm i}P^{*{\rm i}}(K_{\rm i}-K_*)+c_{\rm s}P^{*{\rm s}}(K_{\rm s}-K_*)=0, \tag{2.4}$$

$$c_{\rm i}Q^{*{\rm i}}(G_{\rm i}-G_*)+c_{\rm s}Q^{*{\rm s}}(G_{\rm s}-G_*)=0, \tag{2.5}$$

where K_* and G_* denote the effective moduli and $P^{*{\rm m}}$ and $Q^{*{\rm m}}$ are given in (2.3). Here, $c_{\rm s}=1-c_{\rm i}=p$. Numerical methods are usually used to solve for K_* and G_* (see Hill (1965) and Berryman (1980) for details). Garboczi & Day (1995) showed that, for spherical zero-moduli inclusions, a value of the matrix Poisson ratio $\nu_{\rm s}=0.2$ gave $\nu=0.2$ for all inclusion concentrations that gave non-zero effective moduli. In d dimensions, the critical value of ν was found to be $1/(2d-1)$.

Two other forms of the SCM are relevant to our numerical results. When the inclusions are voids, the SCM predicts a vanishing modulus for $c_{\rm i}\geqslant 0.5$, although many materials remain rigid above this threshold. To address this problem, Christensen (1990) derived an alternative SCM based on concentric spheres embedded in a matrix of unknown moduli. The result is complicated and not reproduced here. Wu (1966) also proposed an SCM for spheroidal inclusions, which we will employ.

The differential effective medium (DEM) theory, reviewed by McLaughlin (1977), provides an alternative to the SCM using a similar philosophy. Suppose that the effective moduli of a composite medium are known to be K_* and G_*. Now, if a small additional concentration of inclusions is added, the change in K_* and G_* is approximated to be that which would arise if a dilute concentration of inclusions were added to a uniform homogeneous matrix with moduli K_* and G_*. This leads to a pair of coupled nonlinear differential equations, which must be solved to find $K^*(c_{\rm i})$ and $G^*(c_{\rm i})$,

$$\frac{{\rm d}K_*}{{\rm d}c_{\rm i}}=P^{*{\rm i}}\frac{K_{\rm i}-K_*}{1-c_{\rm i}}, \qquad K_*(c_{\rm i}=0)=K_{\rm s}, \tag{2.6}$$

$$\frac{{\rm d}G_*}{{\rm d}c_{\rm i}}=Q^{*{\rm i}}\frac{G_{\rm i}-G_*}{1-c_{\rm i}}, \qquad G_*(c_{\rm i}=0)=G_{\rm s}. \tag{2.7}$$

Zimmerman (1994) has shown that $\nu_{\rm s}=0.2$ is also a fixed point for the DEM theory, for any value of inclusion concentration.

Milton (1984) and Norris (1985) have shown that the predictions of the DEM and SCM correspond to the properties of materials with spheroidal inclusions at widely different length-scales. These types of structures are not commonly observed (Christensen 1990). Therefore, except in the dilute limit, neither method can be accurately used to interpret experimental results, or guide the improvement of materials because of the unrealistic microstructural assumptions underlying each kind of theory. Nevertheless, the results are widely used, and until recently (Torquato 1998) were the only predictive theories used for moderate- and high-porosity random interpenetrating porous materials.

(*b*) *Exact bounds and expansions*

There are several kinds of exact bounds that have been derived for the elastic properties of composite materials (see the reviews of Torquato (1991) and Hashin (1983)). If the properties of each phase in a composite are not too dissimilar, the bounds can be quite restrictive. For porous materials, however, the bounds on Poisson's ratio

are no more restrictive than the range guaranteed by the non-negativity of K and G for isotropic materials ($-1 \leqslant \nu \leqslant 0.5$), and the lower bound on E reduces to zero. The upper bound on E is sometimes found to provide a reasonable approximation of the actual property. The most commonly applied bounds for isotropic composites are due to Hashin & Shtrikman (1963). The upper bound E_{u} is

$$\frac{E_{\mathrm{u}}}{E_{\mathrm{s}}} = \frac{p}{1 + C(1-p)}, \qquad C = \frac{(1+\nu_{\mathrm{s}})(13 - 15\nu_{\mathrm{s}})}{2(7 - 5\nu_{\mathrm{s}})}. \tag{2.8}$$

Thus the Hashin–Shtrikman bounds imply $0 < E < E_{\mathrm{u}}$ and $-1 < \nu < 0.5$, and only depend on microstructure via the volume fraction.

It is possible to improve the bound if more statistical information, in the form of N-point correlation functions, is available for the composite. The two-point correlation function $p^{(2)}(r)$ represents the probability that two points, a distance r apart, will fall in the solid phase. The three-point correlation function $p^{(3)}(r, s, t)$ is equal to the probability that three points, distances r, s and t apart, all belong to the solid phase. Bounds that depend on this information are referred to as three-point bounds. The form of the three-point bounds (Beran & Molyneux 1966; Milton & Phan-Thien 1982) is quite complex, but to show their qualitative behaviour we report the result for a porous medium where the solid matrix has a Poisson's ratio of $\nu_{\mathrm{s}} = 0.2$. In this case, the upper bound becomes

$$\frac{E_{\mathrm{u}}}{E_{\mathrm{s}}} = \frac{p}{1 + C(1-p)}, \qquad C = \frac{33\eta + 7\zeta}{5\zeta(9\eta - \zeta)}. \tag{2.9}$$

The three-point bounds on Poisson's ratio are $-1 < \nu < 0.5$. The 'microstructure parameters' ζ and η are determined by (Milton & Phan-Thien 1982)

$$\zeta = \frac{9}{2pq} \int_0^\infty \frac{\mathrm{d}r}{r} \int_0^\infty \frac{\mathrm{d}s}{s} \int_{-1}^1 \mathrm{d}u\, P_2(u) \left(p^{(3)}(r,s,t) - \frac{p^{(2)}(r) p^{(2)}(s)}{p} \right), \tag{2.10}$$

$$\eta = \frac{5\zeta}{21} + \frac{150}{7pq} \int_0^\infty \frac{\mathrm{d}r}{r} \int_0^\infty \frac{\mathrm{d}s}{s} \int_{-1}^1 \mathrm{d}u\, P_4(u) \left(p^{(3)}(r,s,t) - \frac{p^{(2)}(r) p^{(2)}(s)}{p} \right), \tag{2.11}$$

where $t^2 = r^2 + s^2 - 2rsu$ and $P_2(u) = \frac{1}{2}(3u^2 - 1)$ and $P_4(u) = \frac{1}{8}(35u^4 - 30u^2 + 3)$ are Legendre polynomials. A useful numerical listing of these parameters for various systems is given by Torquato (1991).

Torquato (1998) has recently derived predictive formulae for arbitrary composites in the form of exact expansions. For a porous medium, where the solid matrix has a Poisson ratio of $\nu_{\mathrm{s}} = 0.2$, the results simplify to

$$\frac{E}{E_{\mathrm{s}}} = \frac{p}{p + (1-p)C}, \qquad C = \frac{74\zeta + 6\eta}{5\zeta(5\zeta + 3\eta)}, \tag{2.12}$$

$$\nu = \frac{1}{5} + \frac{36(\zeta - \eta)}{25\zeta(5\zeta + 3\eta)} \times \frac{1-p}{p + C(1-p)}. \tag{2.13}$$

A clear advantage of the bounds and expansions is that they incorporate microstructural information, so can be applied to arbitrary composites. In principle, it should be possible to increase the accuracy of both methods by incorporating more statistical information. However, in practice, third-order information is only available

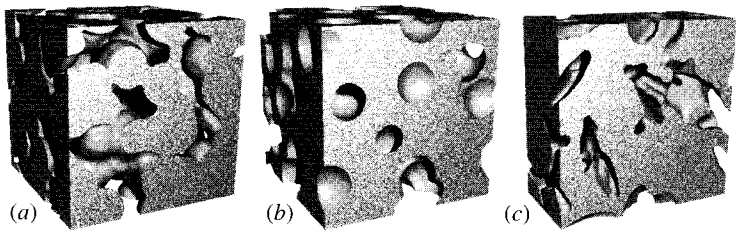

Figure 1. Boolean models of porous media. (*a*) Overlapping solid spheres. (*b*) Spherical pores. (*c*) Oblate spheroidal pores (aspect ratio four).

for a restricted number of models, and it is very difficult to include fourth- or higher-order information. In the truncated forms given above, the results are thought to be accurate for dispersed inclusions (Torquato 1991, 1998, § 3.5). Their accuracy for interpenetrating porous media is not known.

In this section we have described a range of well-known theories for predicting the elastic properties of random porous materials. We have shown that for materials with interconnected pores, none of the theories can be confidently used to predict properties or interpret experimental structure–property relationships. Therefore, in order to apply the theories, it is necessary to check their range of validity. We do this by computationally studying the properties of several well-known models that span a wide range of physically observed microstructure. These numerical results also reveal behaviour that, to a good approximation, is quite similar to rigorous two-dimensional behaviour. The next section introduces the kinds of microstructure considered.

3. Computational methods

(*a*) *Statistical models of microstructure*

We focus on two classes of statistical models for which it is possible to evaluate the microstructure parameters (ζ, η) that occur in the above rigorous theories. Some of the models are based on spheroidal inclusions, and should be relevant to the effective medium theories. The models are also known to mimic some realistic materials (see, for example, Torquato (1991) and Roberts & Knackstedt (1996)).

The most well-known class of statistical models is generated using the 'Boolean' scheme, in which a model is generated by placing objects at random (uncorrelated) points in space. Since the objects are uncorrelated, they can overlap. We consider an overlapping solid sphere model, and its inverse, the overlapping spherical pore or 'Swiss cheese' model (see figure 1). The latter is obtained by creating pores in a solid matrix. These models have a long history (Serra 1988), and the microstructure parameters ζ and η have been evaluated (Helte 1995; Torquato 1991). For comparison with the SCM and DM, we also considered oblate spheroidal pores with an aspect ratio of four (see figure 1). The correlation functions of this model have not been computed to our knowledge.

These Boolean models have percolation thresholds, when the objects are considered to be one phase and the background a second phase. For the overlapping-sphere model, starting with a matrix and adding spheres, the sphere phase percolates at a volume fraction of *ca.* 0.29 (Garboczi *et al.* 1995), while the matrix, which starts out continuous, loses continuity above a sphere volume fraction of *ca.* 0.97 (Torquato

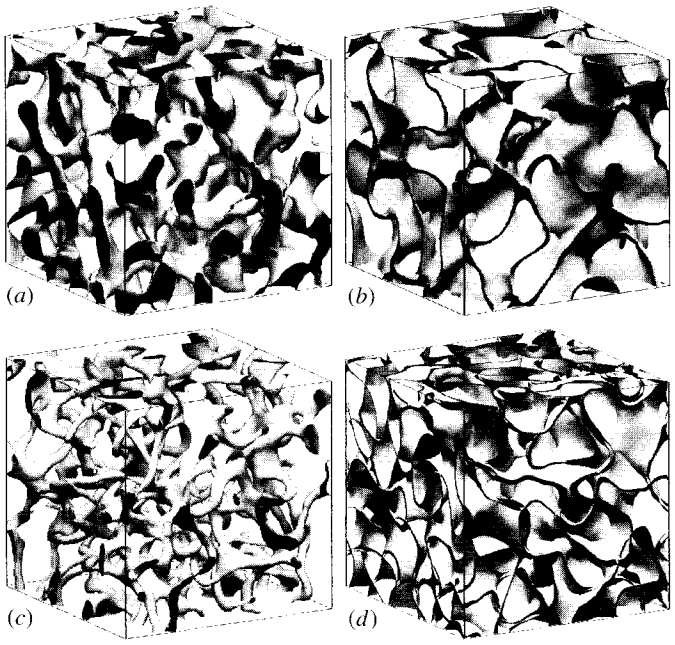

Figure 2. Three-dimensional Gaussian random field models.
(*a*) Single cut. (*b*) Two cut. (*c*) Open-cell intersection. (*d*) Closed-cell union.

1991). When the random objects are prolate or oblate spheroids, the percolation threshold of the objects has been computed (Garboczi *et al.* 1995), but not the matrix, which is a much harder computational problem. The percolation threshold for an oblate object of aspect ratio four (width divided by thickness) is *ca.* 0.2, which is less than that for spheres. The 'isoperimetric' theorem conjectures that for Boolean models with a convex Euclidean shape, the sphere gives the largest volume fraction of overlapping objects at the percolation threshold (Garboczi *et al.* 1995).

It is possible to generate other realistic microstructure models using the level-cut Gaussian random field (GRF) scheme. One starts with a Gaussian random field $y(\boldsymbol{r})$, which assigns a (spatially correlated) random number to each point in space. A two-phase solid-pore model can be defined by letting the region in space where $-\infty < y(\boldsymbol{r}) < \beta$ be solid, while the remainder corresponds to the pore-space (figure 2*a*). The solid fraction has a percolation threshold of *ca.* 0.13 (Roberts & Teubner 1995). Since the model is symmetric, the pores become continuous at *ca.* 0.87. An interesting 'two-cut' GRF model (Berk 1987) can be generated by defining the solid phase to lie in the region $-\beta < y(\boldsymbol{r}) < \beta$ (figure 2*b*). The solid phase of the two-cut model remains connected at all volume fractions, i.e. the percolation threshold is zero. This is because the solid walls of the microstructure do not separate into pieces as the volume fraction decreases, but instead become thinner. Open- and closed-cell models can be obtained from the two-cut version by forming the intersection (figure 2*c*) and union (figure 2*d*) sets of two statistically independent two-cut GRF models (Roberts 1997). By construction, the percolation threshold of the open- and closed-cell models is also zero. It is important to note that in no way can these

random field models be considered as dispersions. However, at dilute porosities, the pores do become disconnected.

The random fields on which the models are based can be entirely specified by the field–field correlation function $G(\boldsymbol{r}_1, \boldsymbol{r}_2) \equiv \langle y(\boldsymbol{r}_1) y(\boldsymbol{r}_2) \rangle$, where $\langle \cdot \rangle$ denotes a volume average. We only consider isotropic and stationary random fields, in which case $G(\boldsymbol{r}_1, \boldsymbol{r}_2) = g(r)$, with $r = |\boldsymbol{r}_1 - \boldsymbol{r}_2|$. We employ the function

$$g(r) = \exp\left(-\frac{r}{\xi}\right)\left(1 + \frac{r}{\xi}\right)\frac{\sin(2\pi r/d)}{(2\pi r/d)}. \tag{3.1}$$

The parameter d controls the position of the maximum in the correlation function, which roughly governs the cell size, while the values of the correlation length ξ and parameter d effect the properties (e.g. roughness) of the pore–solid interface in the level-cut GRF model. We choose the length-scales as $\xi = 6/\pi = 1.91\,\mu\text{m}$ and $d = \sqrt{6} = 2.45\,\mu\text{m}$, which corresponds to a surface area to total volume ratio of $1(\,\mu\text{m})^2/(\mu\text{m})^3$ when $\beta = 0$ for the single-cut GRF model.

To evaluate the bounds, it is necessary to derive the two- and three-point correlation functions of the models. This has been done for the single (Roberts & Teubner 1995) and two-cut (Roberts & Knackstedt 1996) models, although the results are quite cumbersome and not repeated here. The results can be generalized for the open- and closed-cell models as follows. In the usual way, we define an indicator function $\Theta(\boldsymbol{r})$ that is unity in the solid and zero in the pore space. The volume fraction and correlation functions can be defined by

$$\begin{aligned} p &= \langle \Theta(\boldsymbol{r}) \rangle, \\ p^{(2)}_{ij} &= p^{(2)}(r_{ij}) = \langle \Theta(\boldsymbol{r}_i)\Theta(\boldsymbol{r}_j) \rangle, \\ p^{(3)}_{ijk} &= p^{(3)}(r_{ij}, r_{ik}, r_{jk}) = \langle \Theta(\boldsymbol{r}_i)\Theta(\boldsymbol{r}_j)\Theta(\boldsymbol{r}_k) \rangle, \end{aligned}$$

where $r_{ij} = |\boldsymbol{r}_i - \boldsymbol{r}_j|$. The fact that the correlation functions only depend on the distance between points reflects our restriction to statistical stationarity and isotropy. Now suppose we have two independent, but statistically identical, random materials having indicator functions $\Phi(\boldsymbol{r})$ and $\Psi(\boldsymbol{r})$ with volume fraction q, and correlation functions $q^{(2)}_{ij}$ and $q^{(3)}_{ijk}$. If we form the intersection set $\Theta(\boldsymbol{r}) = \Phi(\boldsymbol{r})\Psi(\boldsymbol{r})$, the volume fraction is just

$$p = \langle \Phi(\boldsymbol{r})\Psi(\boldsymbol{r}) \rangle = \langle \Phi(\boldsymbol{r}) \rangle \langle \Psi(\boldsymbol{r}) \rangle = q^2.$$

Similarly, the correlation functions are

$$p^{(2)}_{ij} = (q^{(2)}_{ij})^2 \quad \text{and} \quad p^{(3)}_{ijk} = (q^{(3)}_{ijk})^2.$$

These equations can be used to calculate the correlation functions of the open-cell GRF model, which is defined by the intersection of two two-cut GRF models. For the closed-cell GRF model, the union set is formed by taking

$$\Theta(\boldsymbol{r}) = \Phi(\boldsymbol{r}) + \Psi(\boldsymbol{r}) - \Phi(\boldsymbol{r})\Psi(\boldsymbol{r}).$$

In this case, the volume fraction is $p = q(2 - q)$ and the correlation functions are

$$p^{(2)}_{ij} = 2q^2 + 2(1 - 2q)q^{(2)}_{ij} + (q^{(2)}_{ij})^2, \tag{3.2}$$

$$\begin{aligned} p^{(3)}_{ijk} = {} & 2(q^{(2)}_{ij} + q^{(2)}_{ik} + q^{(2)}_{jk})(q + q^{(3)}_{ijk}) + 2(1 - 3q)q^{(3)}_{ijk} \\ & - (q^{(3)}_{ijk})^2 - 2(q^{(2)}_{ij}q^{(2)}_{ik} + q^{(2)}_{ik}q^{(2)}_{jk} + q^{(2)}_{jk}q^{(2)}_{ij}). \end{aligned} \tag{3.3}$$

Table 1. *The microstructure parameters that appear in three-point bounds and expansions of the bulk and shear moduli, and the electrical conductivity*

(The results for solid spheres were previously calculated by Torquato (1991). Since the spherical pores are the 'inverse' of solid spheres, the parameters are related by $\zeta' = 1 - \zeta$, $\eta' = 1 - \eta$ for $p' = 1 - p$.)

	single-cut GRF		two-cut GRF		open-cell GRF		closed-cell GRF		solid spheres		spherical pores	
p	ζ	η	ζ	η	ζ	η	ζ	η	ζ	η	ζ	η
0.05	0.11	0.07	0.89	0.73	0.48	0.34			0.03	0.04	0.40	0.30
0.10	0.16	0.12	0.84	0.65	0.51	0.36	0.89	0.73	0.06	0.07	0.44	0.34
0.15	0.20	0.16	0.82	0.61	0.53	0.39	0.86	0.69	0.09	0.11	0.48	0.38
0.20	0.25	0.21	0.80	0.59	0.56	0.42	0.84	0.67	0.11	0.15	0.52	0.42
0.30	0.33	0.30	0.79	0.60	0.61	0.48	0.82	0.65	0.17	0.22	0.58	0.49
0.40	0.41	0.40	0.79	0.63	0.66	0.55	0.81	0.66	0.23	0.29	0.65	0.56
0.50	0.50	0.50	0.80	0.67	0.70	0.62	0.80	0.68	0.29	0.37	0.71	0.63
0.60	0.58	0.60	0.82	0.72	0.75	0.69	0.81	0.72	0.35	0.44	0.77	0.71
0.70	0.67	0.70	0.84	0.78	0.80	0.76	0.81	0.76	0.42	0.51	0.83	0.78
0.80	0.75	0.79	0.87	0.84	0.85	0.83	0.82	0.81	0.48	0.58	0.89	0.85
0.90	0.84	0.88	0.90	0.91	0.89	0.90	0.84	0.86	0.56	0.66	0.94	0.93
0.95	0.88	0.92	0.91	0.93	0.91	0.92	0.85	0.89	0.60	0.70	0.97	0.96

The use of intersection and random sets to extend other types of microstructural models has also been employed by Jeulin & Savary (1997).

We used the quadrature method of Roberts & Knackstedt (1996) to evaluate ζ and η for the models described above (excluding the oblate pore model). The results, presented in table 1, have to our knowledge not been previously reported for the open- and closed-cell GRF models. Application of the parameters is not restricted to porous materials. Data in the table can be used to bound the elastic moduli and electrical or thermal conductivity of composite (i.e. non-porous) materials (Torquato 1991). The parameters ζ and η have also been evaluated for several other models (Jeulin & Savary 1997; Torquato 1991).

(*b*) *Finite-element method*

To compute the elastic moduli of the various microstructure models considered, we used a finite-element method that is specially designed to handle arbitrary voxel-based models (Garboczi & Day 1995). A detailed description of the method, and the actual codes are available (Garboczi 1998). In principle, the method provides an exact solution to the equations of elasticity for a body subjected to a macroscopic strain. The resultant average stress in the body is used to calculate the various elastic moduli. In practice, the accuracy of the results is limited by discretization errors (how well a continuum model can be resolved) and statistical noise (the sample size is never 'infinite'). The number of voxels used depends on computer memory and speed. In this study, a maximum of $128 \times 128 \times 128$ voxels are used. The memory requirements are approximately 230 bytes per voxel. There was clearly a trade-off between small well-resolved samples and large poorly resolved samples. For each of

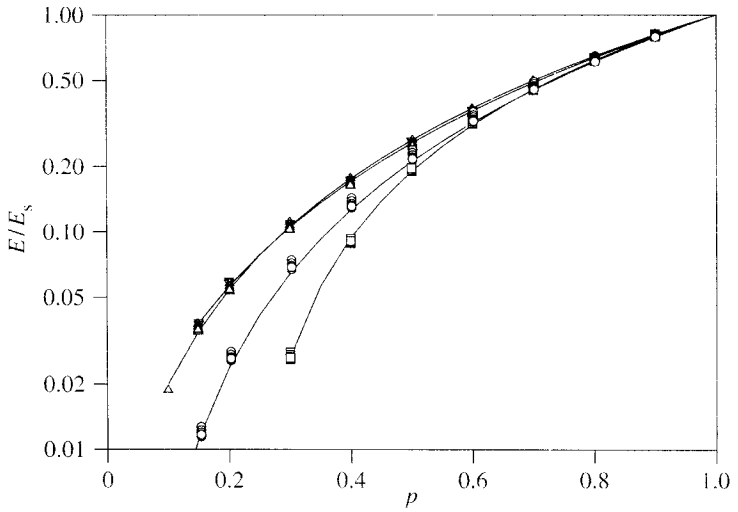

Figure 3. Finite-element data and lines of best fit to equation (4.1) for the four GRF models: single cut (□), two cut (△), open cell (○) and closed cell (▽) (semi-log axes). Data for the two-cut and closed-cell models are nearly coincident.

the models, we conducted a series of tests to find the best sample size. The sample size was approximately five times the pore size. The discretization errors tended to be around a few per cent, and 5–10 independent samples were used to reduce statistical errors to the same order.

4. Elastic property results

For porous materials there exists a percolation threshold (which is zero for some models), below which the structure becomes disconnected. As the threshold is approached, the elastic properties become dependent on small tenuous connections, which are increasingly difficult to resolve. Moreover, for models with a non-zero percolation threshold, percolation theory implies that the connections are separated by an increasing distance, which leads to large statistical errors. Both these factors place a lower limit on the volume fractions at which we could accurately estimate the elastic properties. For models with a finite threshold, we only considered volume fractions such that $p - p_c > 0.1$.

(*a*) *Young's modulus*

Young's modulus of the four GRF models and three Boolean models is shown in figures 3 and 4, respectively. Each data point represents an average over five samples. About 10^4 hours of CPU time, on various workstations, were used to generate the results presented in this paper. Rather than tabulating the data, the results are reported in terms of simple empirical structure–property relations. We found that the data of each of each model could be described by the form

$$\frac{E}{E_s} = \left(\frac{p - p_0}{1 - p_0}\right)^m. \tag{4.1}$$

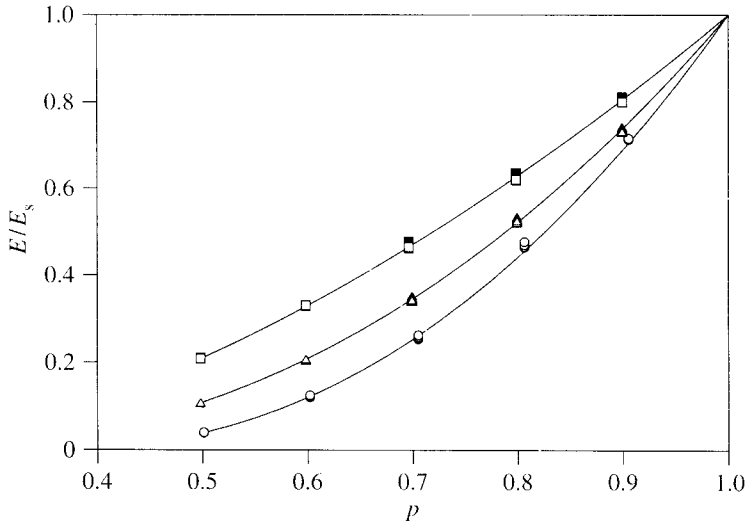

Figure 4. Finite-element data and lines of best fit to equation (4.1) for the three Boolean models: spherical pores (□), oblate spheroidal pores (△), and solid spheres (○).

Table 2. *Simple structure property relations for seven different model porous materials considered in this paper*

(For $p > p_{\min}$, we find that the data can be described by $E/E_s = [(p - p_0)/(1 - p_0)]^m$ to within a few per cent. For the last three models, the data can be extrapolated using the power law $E/E_s = Cp^n$ for $p < p_{\max}$. Poisson's ratio can be approximately described by relation (4.3) with parameters ν_1 and p_1. In certain cases (*), formulae (4.4) and (4.5) should be used if more than a rough estimate is needed.)

		$p < p_{\max}$			$p > p_{\min}$			ν	
model	figure	n	C	$p_{\max}$	m	p_0	$p_{\min}$	ν_1	p_1
solid spheres*	1*a*				2.23	0.348	0.50	0.140	0.528
spherical pores	1*b*				1.65	0.182	0.50	0.221	0.160
oblate pores*	1*c*				2.25	0.202	0.50	0.166	0.396
single-cut GRF	2*a*				1.64	0.214	0.30	0.184	0.258
two-cut GRF	2*b*	1.58	0.717	0.50	2.09	−0.064	0.10	0.220	−0.045
open-cell GRF	2*c*	3.15	4.200	0.20	2.15	0.029	0.20	0.233	0.114
closed-cell GRF*	2*d*	1.54	0.694	0.40	2.30	−0.121	0.15	0.227	−0.029

A nonlinear least-squares fitting program was used to determine p_0 and m. The fitting parameters, obtained for a solid Poisson's ratio of $\nu_s = 0.2$, are reported in table 2. The relative error for any data point is generally around a few per cent or less. Note that the fitting parameter p_0 is not the percolation threshold p_c. For example, $p_0 \approx 0.26$ for the single-cut GRF model, but $p_c \approx 0.13$ (Roberts & Teubner 1995). Clearly, large errors would occur if equation (4.1) were used to extrapolate the data.

By definition, the two-cut, open-cell and closed-cell GRF models have no percolation threshold (i.e. $p_c = 0$). A plot of E/E_s versus p on bi-logarithmic axis (not

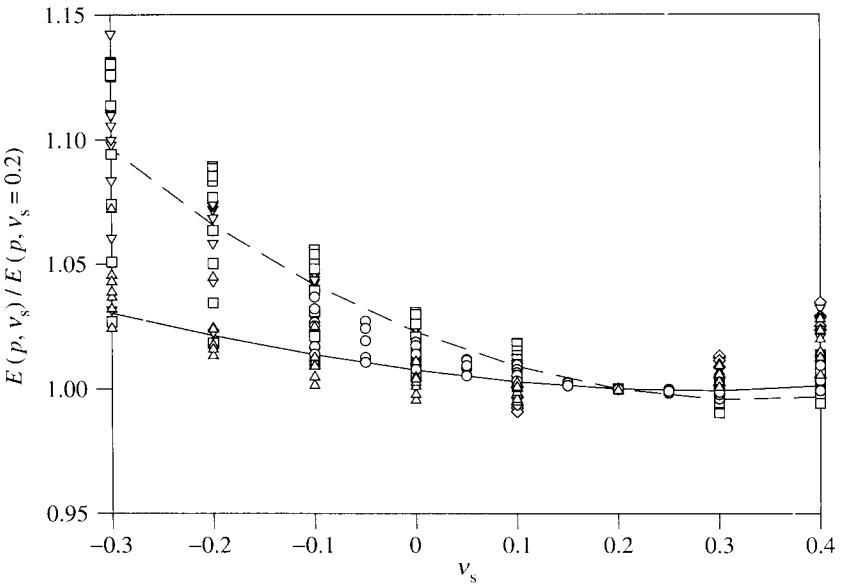

Figure 5. Variation of Young's modulus with solid Poisson's ratio at all solid fractions. Data are shown at all volume fractions studied. Overlapping spheres and oblate spheroids (○), overlapping solid spheres (◇), two-cut and closed-cell GRF models (□), single-cut GRF model (△) and open-cell GRF model (▽). For comparison, the results of the SCM at $p = 0.9$ (solid line) and $p = 0.6$ are shown (dashed line).

shown) revealed a straight line for small p, indicating that data for these models can be extrapolated using the equation

$$\frac{E}{E_s} \approx Cp^n. \tag{4.2}$$

The value of C and n for each model are given in table 2.

In figures 3 and 4, the slight variance observed at each volume fraction corresponds to varying the matrix Poisson ratio. Evidently, as anticipated from the rigorous two-dimensional results, Young's modulus is nearly independent of the solid Poisson ratio, i.e. $E(p, \nu_s) \approx E(p)$. To quantify the weak dependence, we plot $E(p, \nu_s)/E(p, \nu_s = 0.2)$ versus ν_s for the four GRF models and three Boolean models in figure 5. For $0 \leqslant \nu_s \leqslant 0.4$, the relative variance is less than 4%, and we presume that the variance will not be significantly larger for $0.4 < \nu \leqslant 0.5$. Since virtually all solid materials have a solid Poisson ratio in the range $0 \leqslant \nu_s \leqslant 0.5$, we conclude that Young's modulus can practically be regarded as being independent of the solid Poisson ratio. As ν_s decreases, the maximum variance increases to 15% at $\nu_s = -0.3$. In the graph, we also show the SCM for spherical inclusions. The weak dependence of $E(p, \nu_s)$ on ν_s in the data is qualitatively similar to the SCM theory.

In figure 6, we make a quantitative comparison between data for overlapping spherical and oblate pores and the relevant effective medium theories. For $p \geqslant 0.9$ (the dilute limit), all the theories give similar predictions and conform with the data. For both pore shapes, the DEM performs significantly better than the SCM, providing a reasonable prediction for $p \geqslant 0.6$. This might be anticipated from the close similarity between the definition of the models and the assumptions of the differential method.

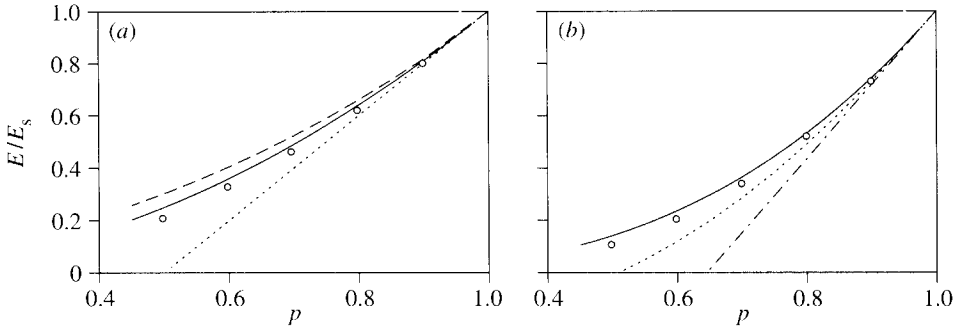

Figure 6. Comparison of various theories to FEM data for overlapping spherical pores (*a*) and oblate spheroidal pores (*b*): SCM (dotted line), DEM (solid line), Christensen's SCM (dashed line), and Wu's SCM (dot–dashed line).

In both the models and DEM, the volume fraction is decreased by adding pores that are uncorrelated to the existing microstucture.

We compare the Hashin–Shtrikman bound, the three-point bound and Torquato's expansion with the FEM data in figure 7. In all cases, the data fall below the bounds. It has been argued (Torquato 1991, § 3.5) that the three-point upper bound and expansion (Torquato 1998) will provide a reasonable prediction if the pores are isolated. This is only true for the closed-cell model, and the data are well predicted by the expansion for $p \geqslant 0.5$. Even when the pores are interconnected, the expansion provides a reasonable prediction for $p \geqslant 0.6$ in all but the case of overlapping solid spheres. Note that large relative differences between the expansion and data occur at lower volume fractions (these become more evident on bi-logarithmic plots).

(*b*) *Poisson's ratio*

In parts (*a*) and (*b*) of figure 8 we plot $\nu(p, \nu_s)$ for the single-cut GRF model as a function of p and ν_s, respectively. Two striking features are evident. In (*a*), a flow diagram is observed, with $\nu(p, \nu_s)$ converging from $\nu(1, \nu_s) = \nu_s$ to a fixed point $\nu_1 \approx 0.2$ as p decreases. The behaviour is very similar to the rigorous behaviour in two dimensions (Day *et al.* 1992). Thorpe & Jasiuk (1992) showed that though the flow behaviour is rigorous, the actual value of the fixed point depends on the microstructure, specifically on how material is removed to achieve the percolation threshold. In (*b*), the lines, which correspond to fixed p, appear to rotate about a 'critical' point, which we call ν^*. On the flow diagram, this point would be represented by a horizontal line, indicating that, for $\nu_s = \nu^*$, Poisson's ratio of the porous material does not depend on the solid fraction, or $\nu(p, \nu^*) \approx \nu^*$. Since both the behaviours in (*a*) and (*b*) exist, evidently ν^* and ν_1 must be identical.

However, the behaviour observed in (*b*) is not a simple consequence of that in (*a*). A flow diagram can exist without all the flow lines, when plotted versus the matrix Poisson ratio, passing through a single point. When this point exists and is found to be on the $\nu = \nu_s$ line, it means that for a given value of the matrix Poisson ratio, the porous body Poisson ratio is the same. As was mentioned in a previous section, this kind of behaviour, along with the flow to a fixed point, is seen in both the SCM and DEM effective medium theories, as well as in the spherical pore dilute limit. The

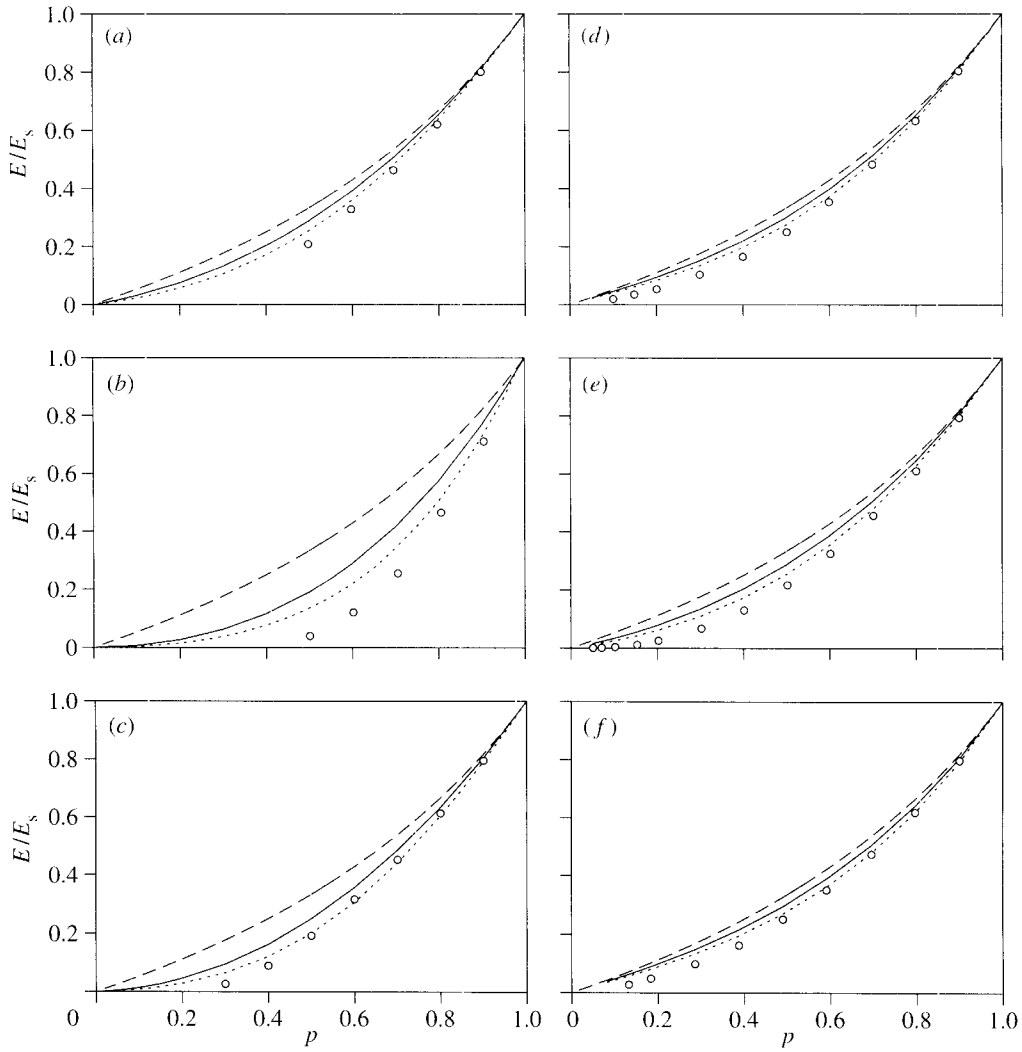

Figure 7. Hashin Shtrikman (dashed line) upper bounds, three-point (solid line) upper bounds and Torquato's expansion (dotted line) versus the finite-element data. The solid Poisson ratio is $\nu_s = 0.2$. (*a*) Overlapping spherical pores. (*b*) Overlapping solid spheres. (*c*) Single-cut GRF. (*d*) Two-cut GRF. (*e*) Open-cell intersection set GRF. (*f*) Closed-cell union set GRF.

present numerical results indicate that this behaviour appears in a realistic porous microstructure as well.

It is important to note at this point that the value of ν^* is the same for each value of p, including the dilute limit ($p \approx 1$). For values of p in this range, the value of ν^* is simply predicted from the dilute limit. This remarkable result implies that the dilute limit can tell us something about the elastic behaviour at the critical point! This is non-intuitive behaviour, and requires thought. If the result only held true for models generated by iteratively using a single defect shape, like a spheroid, one might guess that this shape controlled the microstructure even at porosities approaching

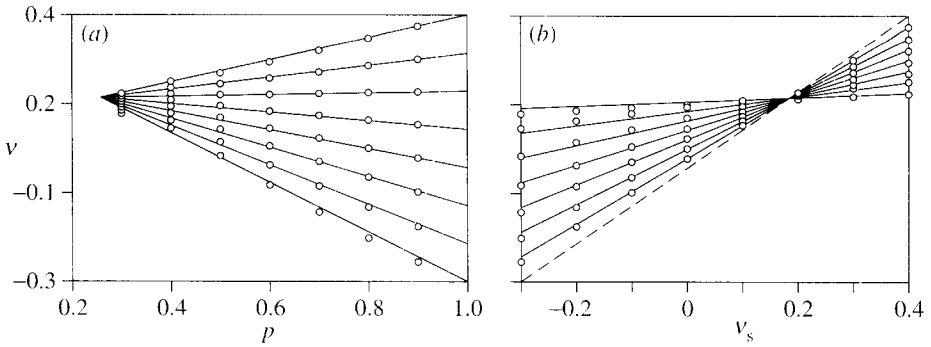

Figure 8. Poisson's ratio $\nu(p, \nu_s)$ of the single-cut GRF model plotted against p and ν_s. In (*a*), the intercept of the data with the vertical axis at $p = 1$ corresponds to ν_s. In (*b*), the dashed line shows the behaviour of a non-porous solid, the next line up (on the $\nu_s = -0.3$ axis) is for $p = 0.9$, and so on, up to $p = 0.3$. At $p = 0.3$, Poisson's ratio is seen to be nearly independent of ν_s. The symbols are data points and the lines are a best fit to equation (4.3).

the critical point. But this result is true, as is shown below, for most of the Gaussian models as well, which are not made from a given shape.

To a reasonable approximation, it appears that $\nu(p, \nu_s)$ is a linear function of both p and ν_s. The above considerations indicate that the data can be described by the relation

$$\nu = \nu_s + \frac{1-p}{1-p_1}(\nu_1 - \nu_s). \tag{4.3}$$

A least-squares procedure was used to determine $p_1 = 0.258$ and $\nu_1 = 0.184$. The function, which is shown in figure 8, is seen to provide a reasonable fit.

In figure 9, we show that Poisson's ratio of the other six models have qualitatively similar flow diagrams. Five of the models show a critical point (not shown) just as in figure 8*b* in plots of ν versus ν_s. In figure 10, it is seen that the closed-cell GRF model, in contrast, does not show a critical point. However, for all six models, there appeared to be a linear relationship between ν and ν_s. The fitting parameters ν_1 and p_1 for each model are given in table 2. In three cases (parts (*b*), (*c*) and (*f*)), some nonlinearity in the parameter p is evident, and equation (4.3) only provides a rough fit. To obtain a better fit, we tested several generalizations of equation (4.3). The form

$$\nu = \nu_s + \left(\frac{1-p}{1-p_1}\right)^k (\nu_1 - \nu_s) \tag{4.4}$$

was able to provide a reasonable fit of the data for overlapping oblate pores ($\nu_1 = 0.161$, $p_1 = 0.041$ and $k = 1.91$) and overlapping solid spheres ($\nu_1 = 0.140$, $p_1 = 0.14$ and $k = 1.22$). In the case of overlapping solid spheres, the error bars (not shown) are significantly larger than in the other models, and on the order of 50% at the largest porosity shown. The results are shown as a dashed line in figure 9*b*, *c*. For the closed-cell GRF model, the simplest form able to fit the data was

$$\nu = A(1-p) + \nu_s(p + B(1-p) + C(1-p)^2), \tag{4.5}$$

with $A = 0.221$, $B = -0.210$ and $C = 0.342$. The results are shown in figures 9*f* and 10. In contrast to equations (4.3) and (4.4), this form does not have a critical

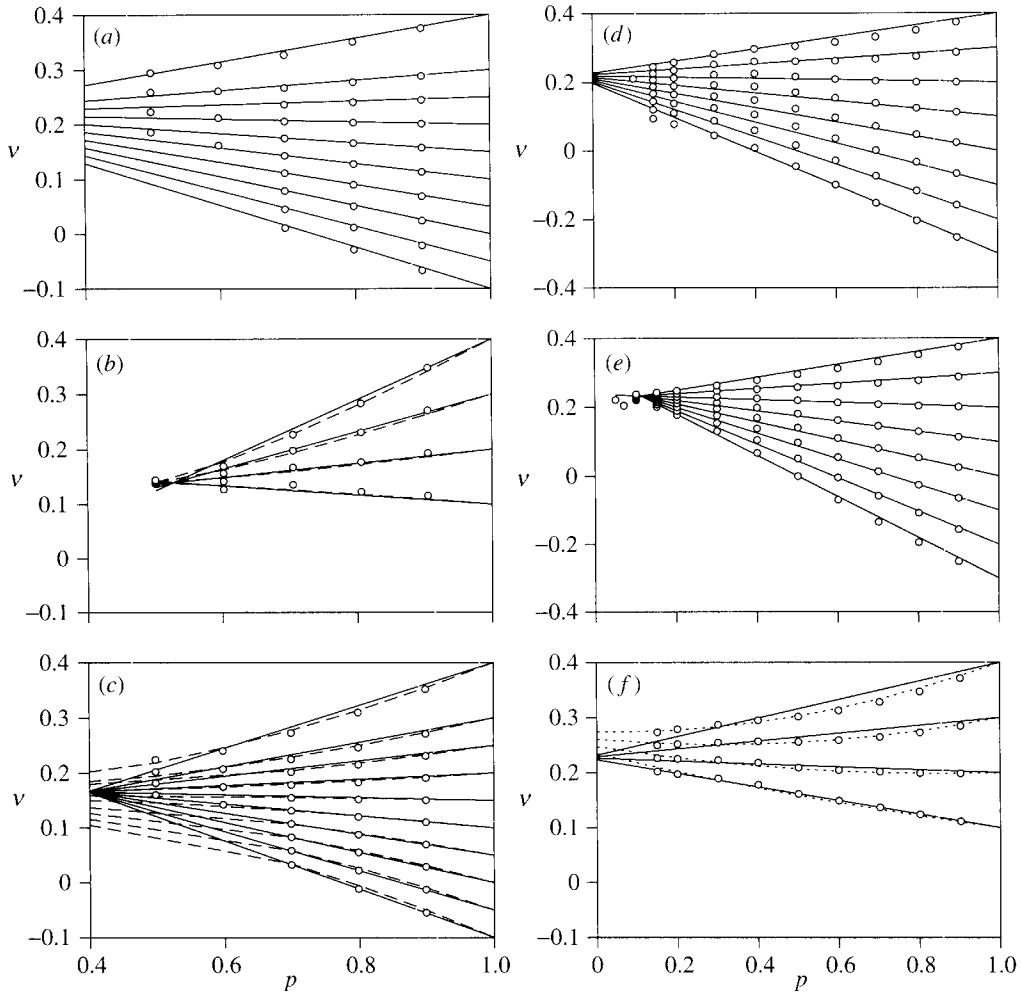

Figure 9. Generic flow pattern behaviour of Poisson's ratio of porous models ν as a function of solid fraction p. (*a*) Overlapping spherical pores. (*b*) Overlapping solid spheres. (*c*) Overlapping oblate spheroidal pores. (*d*) Two-cut GRF. (*e*) Open-cell GRF. (*f*) Closed-cell GRF. The solid lines are numerical fits to equation (4.3). In cases (*b*), (*c*) and (*f*), a better fit is obtained with equation (4.4) (dashed line) or equation (4.5) (dotted line).

point, and extrapolation to $p = 0$ gives $\nu = A + \nu_s(B + C)$, i.e. Poisson's ratio does not become independent of ν_s in this formula. We would expect, however, that real data, if they could be accurately generated in this low-p regime, would indeed flow to a fixed point. Again, we emphasize that the flow to a fixed point is probably more generic behaviour than is the 'rotation' about a critical point, and indeed there is no reason that flow behaviour need imply the critical-point behaviour.

In figure 11 we compare the SCM and DEM results to data for overlapping spherical and oblate pores. As for Young's modulus, all the formulae work well for $p \geqslant 0.9$, the dilute limit, since they are all based on the exact expression in the dilute limit. The DEM performs reasonably well for $p \geqslant 0.7$, outside the dilute limit. The SCM

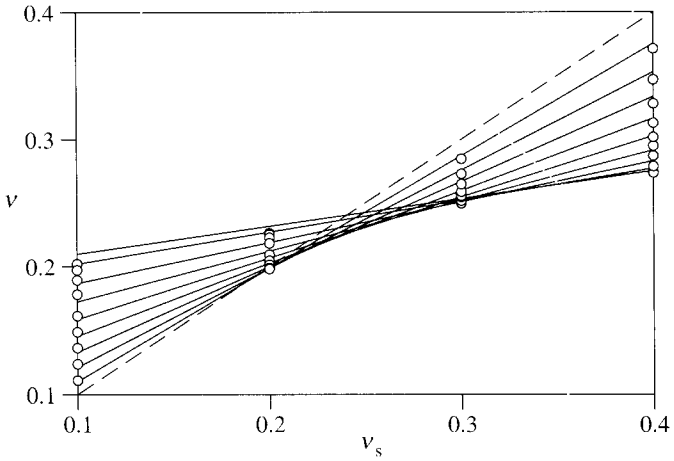

Figure 10. Poisson's ratio of the closed-cell model does not show a critical point.

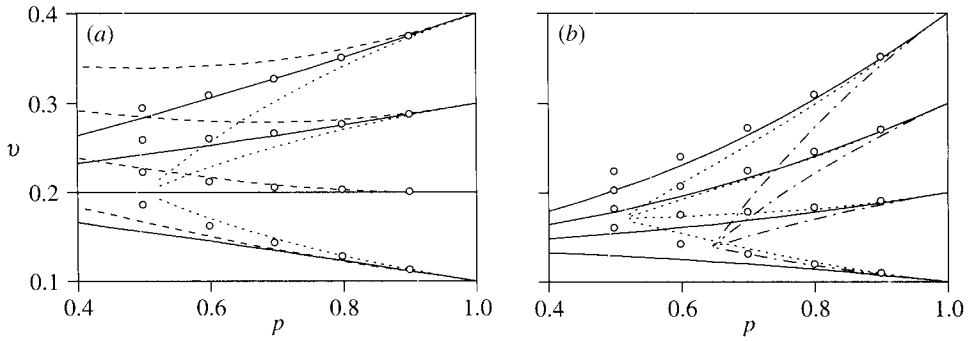

Figure 11. Comparison of various theories to FEM data for overlapping spherical pores (*a*) and oblate spheroidal pores (*b*): SCM (dotted line), DEM (solid line), Christensen's SCM (dashed line) and Wu's SCM (dot–dashed line).

theory, however, badly misrepresents the shape of Poisson's ratio flow diagram for most values of p, at least in part due to the incorrect percolation threshold built into the SCM for spherical pores.

Torquato's truncated expansion is compared with the numerical data in figure 12. This expansion is truncated at the third order because of the difficulty of evaluating the correlation functions needed for the higher-order terms. Apart from the case of solid spheres, the predictions are generally very good for $p \geqslant 0.7$. Since the expansion is not built explicitly upon any dilute limit, it makes sense to use it to compare to the Gaussian random field models. For the closed-cell GRF model, the predictions are very good for a larger range of p ($p \geqslant 0.3$). Note that the closed-cell model has isolated pores by definition. This supports Torquato's hypothesis that the truncated expansion is likely to work for dispersions of isolated pores. However, even when the pores are connected, the stress is still carried by the solid phase, which might be the reason that the expansion seems to work well even for systems with connected pores (S. Torquato 2001, personal communication). At high solid fractions, Torquato's expansion is able to quantitatively reproduce quite subtle nonlinearities in the Pois-

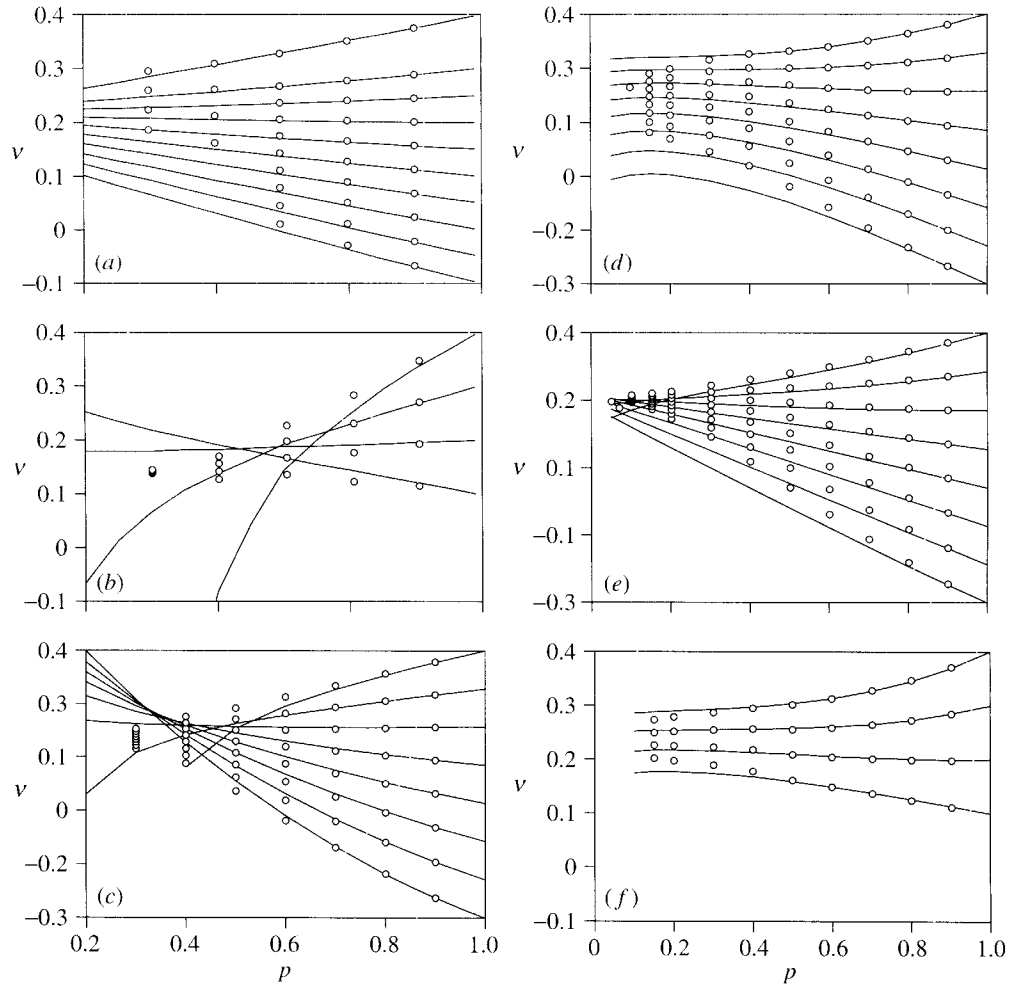

Figure 12. Torquato's expansion (solid line) versus the finite-element data. (*a*) Overlapping spherical pores. (*b*) Overlapping solid spheres. (*c*) Single-cut GRF. (*d*) Two-cut GRF. (*e*) Open-cell intersection set GRF. (*f*) Closed-cell union set GRF.

son ratio plots of the different models, which are a much more stringent test of the theory. In addition to confirming Torquato's results, this provides strong evidence that our FEM, model simulations and method of calculating the microstructural correlation functions and parameters (ζ and η) are quite accurate.

In figures 13 and 14, we show that all but one of the theoretical results exhibit the critical-point behaviour we empirically observed in the data. Christensen's SCM, which is thought to model closed-cell materials when the inclusions are pores (Christensen 1998), does not exhibit a critical point. In this respect, it is similar to our data for the closed-cell GRF model. For spherical pores, the SCM and DEM have exact critical points at $\nu_s = 0.2$ (Garboczi & Day 1995). For oblate pores, Wu's generalizations of the SCM and the DEM have an approximate critical point at $\nu \approx 0.14$. Berryman's generalization of the SCM has an approximate critical point at $\nu \approx 0.17$, in good agreement with the measured value of overlapping oblate pores ($\nu_1 = 0.166$).

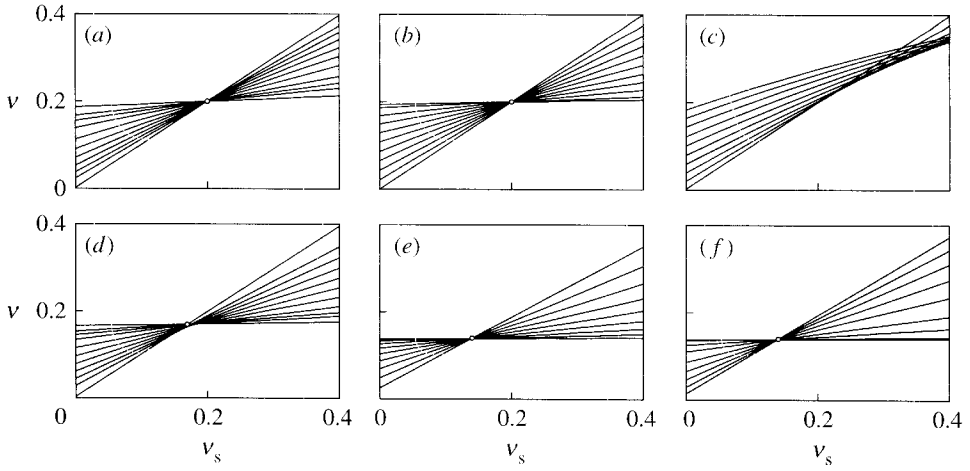

Figure 13. Critical-point behaviour of various effective medium theories. Spherical pores: (*a*) SCM, (*b*) differential method, (*c*) Christensen's SCM. Oblate pores: (*d*) SCM, (*e*) differential method, (*f*) Wu's SCM.

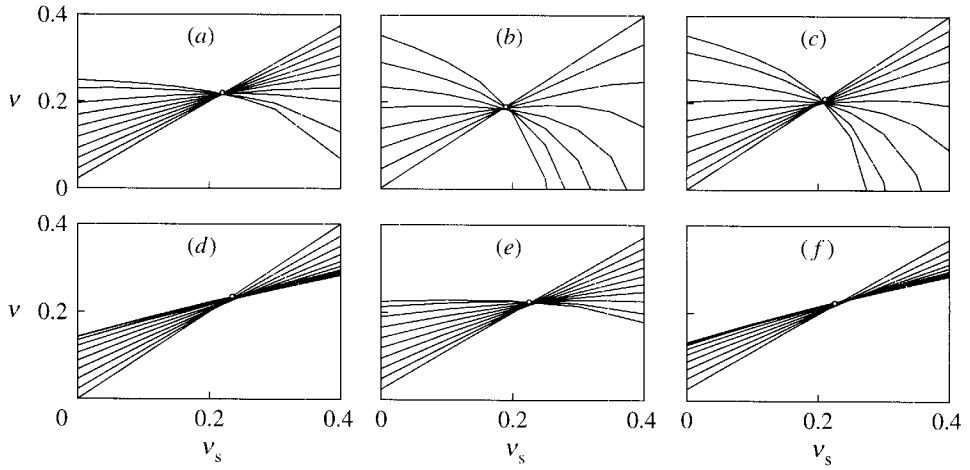

Figure 14. Torquato's expansion has an approximate critical point at $\nu_1 \approx 0.2$. (*a*) Overlapping spherical pores ($\nu_1 = 0.22$). (*b*) Overlapping solid spheres ($\nu_1 = 0.19$). (*c*) Single-cut GRF ($\nu_1 = 0.21$). (*d*) Two-cut GRF ($\nu_1 = 0.23$). (*e*) Open-cell intersection set GRF ($\nu_1 = 0.23$). (*f*) Closed-cell union set GRF ($\nu_1 = 0.23$).

Torquato's expansion revealed an approximate critical point for all six models near $\nu = 0.2$. For overlapping spheres, and the two-cut, open-cell and closed-cell GRF models, the prediction was accurate to within ± 0.01. The form (2.13), in which we have reported Torquato's result, shows the mathematical origin of the critical point. At $\nu_s = 0.2$, $(\nu - 0.2) \propto (\zeta - \eta)$, which is generally quite small (see table 1). It is instructive to linearize Torquato's result $\nu = g_T(p, \nu_s)$ in terms of the variables $\mu = \nu_s - \frac{1}{5}$ and $\theta = \zeta - \eta$, which gives

$$\frac{\nu - \nu_s}{1 - p} = \frac{9\theta - 12(\zeta + 4)\mu}{50\zeta(p\zeta + 2 - 2p)} + O(\theta^2) + O(\mu^2) + O(\mu\theta). \tag{4.6}$$

This form predicts $\nu \approx \nu_s$ at $\mu^* = 3\theta/(4\zeta + 16)$, which is weakly dependent on p via ζ and θ. Surprisingly, the absolute difference between $\nu = \frac{1}{5} + \mu^*$ and exact numerical solution of $\nu - g_T(\nu, p) = 0$ was less than 0.0015 for all models. For $|\theta| \ll |\mu| \ll 1$, equation (4.6) predicts $\nu - \nu_s \propto (\nu_s - \frac{1}{5})$, which corresponds to the cross-over behaviour in figure 14.

5. Discussion and conclusions

We have used the finite-element method to calculate the elastic properties of a wide variety of realistic porous media. Our data confirm that several interesting and related results for two-dimensional materials (Cherkaev *et al.* 1992; Day *et al.* 1992) are very nearly true in three dimensions. These results demonstrate how useful the study of two-dimensional elasticity problems can be to understanding more difficult three-dimensional problems.

We have confirmed that Young's modulus of three-dimensional porous materials is nearly independent of the solid matrix Poisson ratio in the physically realistic range, $0 < \nu_s < 0.5$. Our conclusion supports Christensen's (1993) analysis of Young's modulus based on exact dilute results and effective medium theory. This simplification allowed us to generate simple structure–property relations for the models studied. The results are summarized in table 2. From the empirical formula for Young's modulus and Poisson's ratio, the bulk and shear moduli can be simply calculated. Because the structure–property relations correspond to a known microstructure, the relations can be used to interpret experimental data, and aid in the optimization of porous materials.

We have shown that Poisson's ratio of porous materials generally becomes independent of the solid Poisson ratio near the percolation threshold. This implies that, in this limit, the shape of the solid matrix dominates lateral expansion under uniaxial compression, rather than the material properties of the matrix. Similar to the case of two dimensions (Thorpe & Jasiuk 1992), this Poisson ratio flow behaviour seems ubiquitous, but with the value of the fixed point varying with microstructure. Of the seven models studied, the relatively stiff closed-cell model provided the only exception to this behaviour. The high stiffness may explain why the matrix material retains an influence on the effective Poisson ratio. Interestingly, the limiting value of the Poisson ratio was generally close to $\nu_1 = 0.2$, irrespective of microstructure. This value is predicted by effective medium theory, as was shown in this and other papers (Garboczi & Day 1995), and as seen in figure 13. The numerical data (extrapolated to the apparent percolation threshold) varies in the range $\nu_1 = 0.14$ to 0.28.

In addition to the fixed-point behaviour, the effective Poisson ratio was generally independent of solid fraction if $\nu_s = \nu_1$ (closed-cell models provided the exception). This was clearly evident as a 'critical' point on plots of ν versus ν_s for different solid fractions. When graphed against ν_s, the porous Poisson ratio, for all values of p considered, intersected the $\nu = \nu_s$ line at the same point, $\nu = \nu_s = \nu_1$. We would conjecture that this behaviour shows that the dilute limit, in which ν_1 can be calculated exactly for various shape pores, must play some role in the critical behaviour. This is because $\nu_s = \nu_1 = \nu$, being an invariant for all values of p, implies that the fixed point must be equal to the critical point. Although most of the theories indicate a special significance for the value $\nu = 0.2$, we do not know of a physical

explanation for this behaviour, other than the fact that this is the value that also comes from the dilute spherical pore analytical limit.

By comparing our data with various predictions we were able to establish, on a model-by-model basis, the accuracy of theoretical results at a particular solid fraction. Since the accuracy of theoretical results is not generally known *a priori*, this represents a practical advance. We showed that the differential method gave a reasonable prediction for materials with overlapping spheroidal pores at moderate-to-high solid fractions ($p \geqslant 0.6$). We also found that a recent rigorous result due to Torquato gave reasonable predictions at $p \geqslant 0.7$ for all models tested, with the exception of the overlapping solid spheres model. This model has highly interconnected pores (the pore space is macroscopically connected for $p < 0.97$), which may have been a source of greater error in the expansion. We have calculated the microstructure parameters ζ and η for four models based on Gaussian random fields. These may also be used to evaluate Torquato's expansion for non-porous composites. Generally, porous materials represent a worst-case scenario for predictive methods, leading us to conjecture that the expansion will be quite accurate for composite materials with moderate contrast between the properties of each phase. The accuracy of the expansion at moderate and high solid fractions, using only third-order information, provides impetus to undertake the difficult task (Helte 1995) of including higher-order microstructural information.

US Government work in the public domain in the United States. A.R. thanks the Australian Research Council for financial support. We also thank the HYPERCON High-Performance Concrete programme of the National Institute of Standards and Technology for partial support of this work.

References

Beran, M. & Molyneux, J. 1966 Use of classical variational principles to determine bounds for the effective bulk modulus in heterogeneous media. *Q. Appl. Math.* **24**, 107–118.

Berk, N. F. 1987 Scattering properties of a model bicontinuous structure with a well defined length scale. *Phys. Rev. Lett.* **58**, 2718–2721.

Berryman, J. G. 1980 Long-wavelength propagation in composite elastic media. II. Ellipsoidal inclusions. *J. Acoust. Soc. Am.* **68**, 1820–1831.

Budiansky, B. 1965 On the elastic moduli of some heterogeneous materials. *J. Mech. Phys. Solids* **13**, 223–227.

Cherkaev, A. V., Lurie, K. A. & Milton, G. W. 1992 Invariant properties of the stress in plane elasticity and equivalence classes of composites. *Proc. R. Soc. Lond.* A **438**, 519–529.

Christensen, R. M. 1990 A critical evaluation of a class of micro-mechanics models. *J. Mech. Phys. Solids* **38**, 379–404.

Christensen, R. M. 1993 Effective properties of composite materials containing voids. *Proc. R. Soc. Lond.* A **440**, 461–473.

Christensen, R. M. 1998 Two theoretical elasticity micromechanics models. *J. Elasticity* **50**, 15–25.

Day, A. R., Snyder, K. A., Garboczi, E. J. & Thorpe, M. F. 1992 The elastic moduli of a sheet containing spherical holes. *J. Mech. Phys. Solids* **40**, 1031–1051.

Garboczi, E. J. 1998 NIST Internal report 6269, ch. 2. Available at http://ciks.cbt.nist.gov/garboczi/.

Garboczi, E. J. & Day, A. R. 1995 An algorithm for computing the effective linear elastic properties of heterogeneous materials: three-dimensional results for composites with equal phase Poisson ratios. *J. Mech. Phys. Solids* **43**, 1349–1362.

Garboczi, E. J., Snyder, K. A., Douglas, J. F. & Thorpe, M. F. 1995 Geometrical percolation threshold of overlapping ellipsoids. *Phys. Rev.* E **52**, 819–828.

Hashin, Z. 1983 Analysis of composite-materials—a survey. *J. Appl. Mech.* **50**, 481–505.

Hashin, Z. & Shtrikman, S. 1963 A variational approach to the theory of the elastic behaviour of multiphase materials. *J. Mech. Phys. Solids* **11**, 127–140.

Helte, A. 1995 Fourth order bounds on the effective bulk and shear modulus for a system of fully penetrable spheres. *Proc. R. Soc. Lond.* A **450**, 651–665.

Hill, R. 1965 A self-consistent mechanics of composite materials. *J. Mech. Phys. Solids* **13**, 213–222.

Jeulin, D. & Savary, L. 1997 Effective complex permittivity of random composites. *J. Physique I France* **7**, 1123–1142.

McLaughlin, R. 1977 A study of the differential scheme for composite materials. *Int. J. Engng Sci.* **15**, 237–244.

Milton, G. W. 1984 Microgeometries corresponding exactly with effective medium theories. In *Physics and chemistry of porous media* (ed. D. L. Johnson & P. N. Sen), p. 66. Woodbury, NY: American Institute of Physics.

Milton, G. W. & Phan-Thien, N. 1982 New bounds on effective elastic moduli of two-component materials. *Proc. R. Soc. Lond.* A **380**, 305–331.

Norris, A. N. 1985 A differential scheme for the effective moduli of composites. *Mech. Mater.* **4**, 1–16.

Roberts, A. P. 1997 Morphology and thermal conductivity of model organic aerogels. *Phys. Rev.* E **55**, 1286–1289.

Roberts, A. P. & Garboczi, E. J. 1999 Elastic properties of a tungsten–silver composite by reconstruction and computation. *J. Mech. Phys. Solids* **47**, 2029–2055.

Roberts, A. P. & Knackstedt, M. A. 1996 Structure-property correlations in model composite materials. *Phys. Rev.* E **54**, 2313–2328.

Roberts, A. P. & Teubner, M. 1995 Transport properties of heterogeneous materials derived from Gaussian random fields: bounds and simulation. *Phys. Rev.* E **51**, 4141–4154.

Serra, J. 1988 *Image analysis and mathematical morphology.* Academic.

Thorpe, M. F. & Jasiuk, I. 1992 New results in the theory of elasticity for two-dimensional composites. *Proc. R. Soc. Lond.* A **438**, 531–544.

Torquato, S. 1991 Random heterogeneous media: microstructure and improved bounds on effective properties. *Appl. Mech. Rev.* **44**, 37–76.

Torquato, S. 1998 Effective stiffness tensor of composite media. II. Applications to isotropic dispersions. *J. Mech. Phys. Solids* **46**, 1411–1440.

Wu, T. T. 1966 The effect of inclusion shape on the elastic moduli of a two-phase material. *Int. J. Solids Struct.* **2**, 1–8.

Zimmerman, R. W. 1994 Behaviour of the Poisson ratio of a two-phase composite materials in the high-concentration limit. *Appl. Mech. Rev.* **47**, S38–S44.